Journal of Materials Chemistry B

Accepted Manuscript

ROYAL SOCIETY OF CHEMISTRY

www.rsc.org/materialsB

Folate-targeted Perfluorohexane Nanoparticles Carrying Bismuth Sulfide for Use in US/CT Dual-Mode Imaging and Synergistic High-intensity Focused Ultrasound Ablation of Cervical Cancer

Di Zhou [a], Chuanfei Li[b], Minyu He[a], Ming Ma[c], Pan Li[a], Yuping Gong[a], Haitao Ran[a], Zhibiao Wang[d], Zhigang Wang[a] Yuanyi Zheng[a*], Yang Sun[a*]*

[a]Second Affiliated Hospital, Institute of Ultrasound Imaging, Chongqing Medical University, Chongqing, 400010, P. R. China

[b]The Second Affiliated Hospital of Chongqing Medical University，Chongqing, 400010, P. R. China

[c]State Laboratory of High Performance Ceramics and Microstructures, Chinese Academy of Sciences, Shanghai, 200050, P. R. China.

[d]College of Biomedical Engineering, Chongqing Medical University, Chongqing, 400016, P. R. China

* Corresponding author:

Prof. Zhigang Wang, Prof. Yuanyi Zheng , Prof. Yang Sun

Second Affliated Hospital, Institute of Ultrasound Imaging, Chongqing Medical University,Linjiang Road 76, Chongqing, 400010, P.R. China

E-mail:wzg62942443@163.com(Zhigang Wang), zhengyuanyi@gmail.com(Yuanyi Zheng), sy19850905@126.com(Yang Sun)

ABSTRACT: The integration of multimodal contrast-enhanced diagnostic imaging techniques with noninvasive high-intensity focused ultrasound (HIFU) synergistic therapy could allow the real-time guidance, monitoring and assessment of cancer therapeutic procedures and effects. Herein, we investigated the use of folate-targeted perfluorohexane nanoparticles carrying bismuth sulfide (Bi_2S_3) (FLBS-PFH-NPs) as a dual-modal contrast agent for ultrasound/computed tomography (US/CT) imaging and aimed to targeted increase the therapeutic efficiency of HIFU for cervical cancer treatment. FLBS-PFH-NPs were fabricated to investigate their potential as theranostic nanoplatforms. Their characteristics, phase-transformation properties, and cytotoxicities were also studied in this work. Sequential modifications with polyethylene glycol (PEG) endowed the

FLBS-PFH-NPs with excellent stability and good biocompatibility. Moreover, compared with non-folate-targeted group, the experimental group that received folate ligands had higher internalization efficiency and specificity. We sequentially investigated the effectiveness of these nanoparticles when used as dual-modal contrast agents in US and CT imaging *in vitro* and *in vivo*. The capsulated PFH could undergo a phase transition and form microbubbles upon ultrasonic irradiation, which enhanced the cavitation effects of HIFU in the targeted regions. Then, they were applied to *in vitro* bovine liver samples; the composite nanoparticles improved the efficiency of HIFU synergistic ablation. Our *in vivo* results also revealed that the coagulative necrosis volumes of tumors in the folate-targeted groups with HIFU ablation after FLBS-PFH-NP administration were significantly greater than those of the non-folate-targeted groups. Pathological and immunohistochemical examinations were systematically performed to further verify these results. In brief, FLBS-PFH-NPs may serve as a dual-modal contrast agent to enhance US/CT imaging and HIFU synergistic therapy.Novel nanosized multifunctional contrast agents would be of great value and could provide more comprehensive diagnostic information for more accurate and effective cancer therapy.

KEYWORDS: Bismuth sulfide; perfluorohexane; folate; ultrasound; computed tomography; multifunctional; HIFU.

1. INTRODUCTION

Early detection and treatment of cancer are critical factors for a favorable prognosis. The development of cancer theranostics that use nanosized multifunctional contrast agents (NMCAs) is an emerging field. The emergence of NMCAs has opened up new possibilities for precisely visualizing biological and physiological processes at the molecular and cellular levels in real time and improving the synergistic efficacy of therapy. [1] NMCAs are useful not only for acquiring complementary biological information from multimodal imaging but also for delivering therapeutic agents to cancer cells, making cancer theranostics possible. [2-3] Currently, tThe development of cancer theranostics that use hass in real time and improving the not only for acquiringbut also for

deliveringCurrently, he main noninvasive diagnostic imaging approaches are including ultrasound (US), computed tomography (CT), magnetic resonance imaging (MRI), and single-photon emission computed tomography (SPECT). Each imaging modality has its own advantages and limitations. Two or more biomedical imaging methods are usually combined to obtain reliable diagnostic results after the administration of therapeutics. Therefore, the idea of using multimodal imaging modalities in conjunction with therapeutics has attracted the attention of researchers.[4]

US imaging is a clinically used diagnostic method due to its desirable features, such as its real-time monitoring capability, high safety and sensitivity, low cost, availability and portability.[5] However, the resolution of US is relatively poor compared to that of other imaging techniques, and gas-filled organs or bones, such as the gastrointestinal tract and the craniocerebrum, interfere with the imaging process. The shortcomings of US imaging are the merits of CT imaging, which has excellent spatial resolution based on density. CT imaging is also not disrupted by gas or bone, has unlimited tissue penetration depth, is cost effective, and allows the facile 3-D visual reconstruction of tissues. In brief, CT is beneficial when accurate anatomic information must be obtained. However, because of the low sensitivity of CT imaging and the poor soft tissue contrast [6], CT scans must be repeated, which exposes patients to relatively high doses of irradiation. Thus, US/CT dual-mode imaging is a promising method for improving real-time imaging contrast, gaining anatomic information for clinical applications, and developing better diagnostics to guide and monitor tumor ablation. Moreover, numerous evident superiorities over the multimodal imaging has attracted extensive interest in the design and development NMCAs , which could unify multimodal detectability and therapeutics in the same agent while not inducing additional stress on blood clearance mechanisms.

US microbubbles that carry CT contrast agents have been employed in the development of US/CT or US/MRI multimodal imaging agents. Barrefelt AA et al reported that 99mTc-labeled magnetic microbubbles could obviously enhance US, SPECT/CT and MR imaging. [7] Torkel B. Brismar et al observed similar results and reported that microbubbles coupled with magnetic nanoparticles could synchronously improve the echo intensity and signal of US/MRI imaging. [8] Besides, Nutte Teraphongphom et al displayed that

microbubbles encapsulating quantum dots, magnetic iron oxide nanoparticles, or gold nanoparticles could create bimodality platforms.[9] Microbubbles have been shown to enhance the echo signals of US imaging because they can serve as US reflectors by resonating at diagnostic frequencies. [10] However, their large sizes prevent their use in extravascular imaging applications and make them easily capturable by the reticule endothelial system (RES), which would result in short circulation times and low levels of accumulation in tumors. [11-12] Furthermore, gas-filled microbubbles are unstable, which significantly limits their use in multimodal imaging. To solve these issues, we aimed to combine the advantages of PFH and Bi_2S_3 to prepare a nanosized phase-transformable lipid agents. It was nanosized, stable at room temperature and could be change into bubbles after heating, which could improve US echo intensities in US imaging.

To overcome the instability of these microbubbles, Meng Ao et al successfully prepared Gd-diethylenetriamine pentaacetic acid (DTPA)-loaded polylactic-co-glycolic acid (PLGA) microbubbles for US/MRI imaging and demonstrated that they were much more stable than US microbubbles. [13] The emergence of multifunctional polymer microbubbles has provided high resistance against compression and excellent stability; nevertheless, pure polymer microbubbles have limited ability to improve contrast-enhanced US imaging because their thick and rigid shells decrease the compressibility of the microbubbles and lead to a reduction in backscattering signals. Perfluorocarbons (PFCs) have shown potential for multimodal imaging [14] due to their safety, biocompatibility, high density, low acoustic velocity, low surface tension, hydrophobicity and lipophobicity. Recently, it was revealed that gold nanoshell perfluorooctylbromide (PFOB) nanocapsules could enhance dual US/CT imaging signals.[15] The liquid PFC nanoparticles were stable at room temperature and were nanosized, which allowed them to penetrate through vascular endothelial gaps to tumor tissues. However, the enhancement effects of nanosized liquid PFC nanocapsules in US imaging were far less than those observed for microbubbles. This difference occurred because the nanocapsules mainly utilized aggregates to improve imaging contrast, whereas microbubbles could make use of nonlinear backscattering effects. To overcome the drawbacks and preserve the advantages of liquid PFC nanoparticles, researchers

utilized the liquid-gas phase transition ability of liquid PFCs. Perfluorohexane (PFH) is a type of PFC that is highly biocompatible and has the most adequate phase-transition temperature (56 °C) of all of the known liquid PFCs; consequently, PFH has been extensively studied in clinical trials.[16] PFH is a liquid, is stable at room temperature and is able to change into a gas upon heating or exposure to an US irradiation-induced local temperature increase. The generated PFH bubbles have been shown to improve US echo intensities in US imaging.[17]

For the US/CT dual imaging agents, iodine is a commonly used CT contrast agent, but it has several limitations: (a) short imaging times that are attributed to rapid renal clearance, thus limiting their applications to target imaging and angiography, (b) the necessity for large doses of iodine-based compounds to obtain satisfactory contrast, which may give rise to adverse effects, such as renal toxicity,[18] and (c) the possible induction of anaphylactic reactions and vascular permeation.[19-20] Recently, a new CT contrast agent based on bismuth sulfide (Bi_2S_3) nanoparticles was developed. Bi_2S_3 is composed of metal elements with high atomic numbers that possess high X-ray attenuation coefficients (fivefold better than that of iodine), which may improve CT contrast.[21-22] In particular, compared to traditional iodine-based imaging agents, Bi_2S_3 has several desirable characteristics, such as low toxicity, cost effectiveness, small size, long circulation times and the ability to accept functional surface modifications. [23-24] Anna L. Brown et al [25] gained the similar characteristics and revealed that ultrahigh payload Bismuth nanopartciles have promising physical and cytotoxicological properties for use as x-rays contrast agents. However, it could only served as single imaging model with imaging disadvantages.

Hence, the development of a novel US/CT dual imaging agent using PFH and Bi_2S_3 nanoparticles to simultaneously improve the sensitivities of US and CT imaging and overcome their limitations is of great importance. Notably, these types of imaging agents would be exceptionally attractive if they enabled the combination of multimodal imaging and synergistic therapies for cancer.

Generally, hysterectomy-based surgery and postoperative adjuvant radiotherapy (RT) or chemotherapy are used to treat cervical cancer.[26-27] However, surgery is invasive and is

reserved mainly for the removal of early-stage tumors. Moreover, RT and chemotherapy can damage normal tissues and cause adverse effects. At the same time, conservation of uterine function is an attractive option for patients with cervical cancer. Previous studies revealed that substantial impediments were left unresolved after treatment with cervical cancer therapeutics, such as the unattainable early detection of malignant cells circulating in blood or small tumors, the temporal separation of diagnostic and therapeutic clinical phases, and the poor effects of non-specific chemotherapy drug treatments against multidrug-resistant cancer cells.[28-30]

Therefore, high-intensity focused ultrasound (HIFU) has attracted extensive attention from medical and biological researchers as a representative method for real-time monitoring and noninvasive therapy.[31] The main mechanisms of HIFU are thermal and cavitation effects. Thermal effects promote therapeutic target tissue necrosis by focusing and depositing ultrasonic energy and rapidly raising the tissue temperature.[32] Cavitation effects result from the cavitation bubbles produced by liquids after ultrasonic vibration; the bubbles gradually increase in size and undergo a drastic rupture process. This process could change the function and structure of cell membranes, thus killing tumor cells through the shock wave and jet flow produced by acoustic cavitation. HIFU ablation has been noted as a feasible, effective, non-irradiative, and complication-free treatment; it could be used for clinical tumor treatment[33] and holds great potential for treating gynecologic malignancies. Nevertheless, several issues must be addressed prior to its clinical use. Ultrasonic energy attenuates exponentially with increases in the tissue depth. Moreover, high-speed blood flow can remove heat energy and decrease the therapeutic efficacy of HIFU. Additionally, side effects, such as skin burns, can occur due to the high acoustic power levels of the US propagation channels.

To solve these issues, we aimed to combine the advantages of PFH and Bi_2S_3 to prepare a nanosized phase-transformable lipid agent linked to folate (FLBS-PFH-NPs) that could penetrate through the leaky vasculature of tumors and accumulate in them, thereby improving the therapeutic efficacy of HIFU. Lipid nanoparticles have high penetrability, high drug-loading capacity, long circulation times, and good imaging properties and are safe for medical applications.[34] Moreover, PFH is temperature sensitive

and can change into cavitation bubbles upon ultrasonic vibration in targeted regions to enhance cavitation effects. Bi_2S_3 can change the acoustic impedance and acoustic environments of tissues and can enhance ultrasonic energy absorption and convert it into thermal energy, which would improve the thermal effects. Folate is a small molecule that is present in the human body and may not induce an unexpected immune response.[35] Furthermore, folate receptors are highly expressed in most malignant tumors, including ovarian cancer, cervical cancer, endometrial cancer, and breast cancer,[36-37] and represent an ideal target for cancer treatment. Therefore, FLBS-PFH-NPs could specifically target tumors and increase the accumulation of nanoparticles in these tumors.

Interestingly, the simultaneous combination of multiple functions, such as active tumor targeting, imaging ultrasensitivity and therapy, in one system represents a new paradigm in nanomedicine. Therefore, we aimed to prepare a novel folate-targeting multifunctional lipid contrast agent that combined Bi_2S_3 nanoparticles and PFH in one nanoplatform. The FLBS-PFH-NPs not only offered US or CT imaging information for precise diagnoses but also were able to enhance the therapeutic efficiency of imaging-guided HIFU. The prepared FLBS-PFH-NPs were nanostructures with liquid cores composed of PFH, where the lipid shell was coated with Bi_2S_3. These nanosized phase-transformable emulsion droplets could transport through blood pools, penetrate vasculature and accumulate in tumor tissues. Concurrently, they could actively recognize tumor cells and be efficiently absorbed after surface-modification with folate. In addition, FLBS-PFH-NPs could transform into microbubbles in targeted regions after being heated or subjected to US irradiation to enhance the US imaging and HIFU therapeutic effects. More importantly, we demonstrated that the combination of CT and US based on this theranostic platform was beneficial for deep imaging depth, high spatial resolution to soft tissue and bone as well as real-time imaging. Consequently, the development of FLBS-PFH-NPs offers a tool for precise diagnoses, imaging guidance and therapy.

2. EXPERIMENTAL SECTION

2.1. Materials

Lipids compounds including phosphatidylcholine (DPPC), glycerol phospholipids

(DPPG), phosphatidylethanolamine-polyethyleneglycol (DSPE-PEG), 2-distearoyl-sn-glycero-3-phosphoethanolamine-N-[amino(polyethyleneglycol)-2000]-folate[DSPE-PEG(2000)-folate] and cholesterol (CH) were obtained from Avanti Polar Lipids, Inc, Alabaster, AL. Bismuth sulfide nanoparticles prepared according to related literatures[38-43] were supplied by State Laboratory of High Performance Ceramics and Microstructures, Chinese Academy of Sciences, Shanghai. Perfluorohexane (PFH), fluorescence dye, 1,1'-dioctadecyl-3,3,3',3'-tetramethylindocarbocyanine perchlorate (DiI) and 3,3′-dioctadecyloxacarbocyanine perchlorate (DiO) were purchased from Sigma–Aldrich Chemical Co. (St. Louis, MO). Chloroform ($CHCl_3$) was acquired from Fishers Scientific (Newton, NJ). Phosphate buffered saline (PBS) was prepared by Life Sciences Institute of Chongqing Medical University. In all experiments, the deionized water used was generated by Millipore Infinity water purification system (Milipore, US).

2.2. Preparation of FLBS-PFH-NPs

Folate-targeted liposomes-encapsulated Bi_2S_3 and PFH nanoparticles (FLBS-PFH-NPs) were fabricated by film hydration method coupled with double emulsion method. At first, 100 mg of lipids compound including DPPC, DSPE-PEG (2000)-folate, DPPG, and CH with mass ratio of 5:2:1.5:1.5 were dissolved in 10 ml $CHCl_3$ till clear. Then, 100 μl of Bi_2S_3 solution (10 mg/ml) were added to the $CHCl_3$ solution. The mixture was transferred into the rotary evaporator (Yarong Inc, Shanghai,China) and rotated at 55 rpm and 45 ℃ to clear the $CHCl_3$.The thin lipid film formed was rehydrated with 5 mL PBS to generate a brown suspension. The suspension was then dispersed with a high-speed homogenizer (FJ300-SH, Shanghai, China) for 5 min after drop-by-drop addition 500μL PFH. The secondary emulsion was performed by means of ultrasonic oscillator (SONICS & MATERALS Inc:USA) for 5 min in the ice-cold environment (0 °C). Finally, the mixture nanoemulsions were harvested and centrifuged (Eppendorf, German) at 4500 rpm for 5min and washed with deionized water for three times to sweep away dissociative Bi_2S_3, lipids and PFH. The final emulsion was collected and stored at 4 °C for further use. DSPE-PEG was employed to instead of the DSPE-PEG (2000)-folate in the process to prepare the non-targeted liposomes-encapsulated Bi_2S_3 and PFH nanoparticles

(NLBS-PFH-NPs). Again, liposomes-encapsulated PFH nanoparticles (L-PFH-NPs) were prepared through the same process except for adding Bi_2S_3 particles. Fluorescent nanoemulsions were obtained according to the above procedure except that the DiI was blended in the lipids solution.

2.3. Characterization of FLBS-PFH-NPs

FLBS-PFH-NPs were imaged using a light microscope (LM, Olympus CKX41, Tokyo, Japan), transmission electron microscope (TEM, Hitachi H-600, Tokyo, Japan). Fluorescence images were recorded using an inverted fluorescence microscope (Olympus IX53, Tokyo, Japan). Average sizes and electric potentials were measured by dynamic light scattering (DLS) (Zeta SIZER 3000HS; Malvern, USA). The existence of Bi_2S_3 nanoparticles encapsulated in the microspheres was checked using TEM and an energy dispersive spectrometer (EDS). The presence of Bi_2S_3 nanoparticles coated on the FLBS-PFH-NPs was confirmed with a crystal structure obtained by X-ray diffraction (XRD). Moreover, the concentrations of bismuth after adding different volumes (200, 400, 600, 800, and 1000 μL) of Bi_2S_3 during the preparation of FLBS-PFH-NPs were detected using an inductively coupled plasma optical emission spectrometer (ICP-OES).

2.4. *In vitro* phase transformation of FLBS-PFH-NPs

First, we observed the phase transformation of FLBS-PFH-NPs after thermal evaporation using an inverted fluorescence microscope. A drop of a diluted FLBS-PFH-NP solution was placed on a glass slide, which was covered with a cover slip and placed on a heating plate. The heating plate was then fixed on the microscope stage of the inverted fluorescence microscope. Phase changes were observed with increases in the environment temperature. Microscopy images and temperatures were recorded before and after heating. A 2 mL fraction of the FLBS-PFH-NP solution was diluted with double-distilled water and was loaded in epoxy epoxide (EP) pipes. Then, the EP pipes were fastened to a pair of tweezers and immersed in the degassed water channel of a JC200 HIFU tumor treatment system (Chongqing HIFU Medical Technology Limited-liability Company). US images in B and contrast mode were collected before and after HIFU irradiation. The corresponding acoustic intensities and gray values were

measured using a "DFY" ultrasonic quantitative analysis diagnostic system ("DFY" System, Chongqing Medical University, Chongqing, China). We used the following HIFU ablation parameters for our experiment: exposure duration of 2 s and acoustic power levels of 60, 90, 120, 150 or 180 W.

2.5. Cell culture

Human hepatic cells L02 were cultured in RPMI 1640 medium with 10% FBS and 1% penicillin–streptomycin. Cells from the HeLa cervical cancer cell line were cultured in DMEM medium supplemented with 10% FBS, penicillin (100 U/mL) and streptomycin (100 U/mL). The cell incubator contained 5% carbon dioxide and 95% air in a humidified atmosphere at 37 °C. The HeLa monolayer cells were detached with trypsin when needed.

2.6. Evaluations of the *in vitro* and *in vivo* biosafety of the FLBS-PFH-NPs

2.6.1. MTT assay

A methyl thiazolyl tetrazolium (MTT) assay was used to estimate the cytotoxicity caused by FLBS-PFH-NP uptake, as previously described.[44] Normal human hepatic cells were incubated with fresh medium including FLBS-PFH-NPs at different Bi concentrations (1.0, 2.0, 3.0, 4.0, and 5.0 mg/mL). Two groups of L02 cells were incubated with the FLBS-PFH-NPs for 24 h and 48 h. Absorbances were measured using a microplate reader (BIORAD 680, Hercules, CA, USA) at 490 nm. The inhibition rates were calculated according to the following formula:[45-46]

Growth inhibition rate (%) = (1-Absorbance of experimental group/Absorbance of control group) × 100%

2.6.2. Cell cycle characterization

The cell cycles were evaluated using flow cytometry. L02 cells (1×10^6 cells/mL) were incubated with FLBS-PFH-NPs at a Bi concentration of 5.0 mg/mL for 24 h in RPMI 1640 medium containing 10% FBS and 1% penicillin–streptomycin. Cells in the exponential growth phase were then trypsinized, centrifuged and washed with PBS (0.01

M) twice. PBS was used a negative control for each incubation period. Subsequently, the cells were stained with 50 *i*g/mL of propidium iodide (PI) and 100 μL/mL of RNase A for 30 min in the dark at 37 °C. The L02 cell cycles were analyzed by measuring the DNA content in the PI-stained cells. Finally, the percentages of cells in the G1/G0, S, and G2/M phases were detected with flow cytometry using Cell Quest.

2.6.3. Apoptosis characterization

Apoptosis was assessed using flow cytometry. L02 cells (1×10^6 cells/mL) were incubated with FLBS-PFH-NPs at a Bi concentration of 5.0 mg/mL for 24 h in RPMI 1640 medium containing 10% FBS and 1% penicillin–streptomycin. Cells in the exponential growth phase were trypsinized, centrifuged and washed with PBS twice. PBS was used as a negative control for each incubation period. Then, the cells were fixed with 195 μL of Annexin-PE binding buffer, incubated in the dark for 20 min at room temperature, and then mixed with 5 μL of an AnnexinV-PE solution. Finally, we characterized the apoptosis with flow cytometry using Cell Quest.[47]

2.6.4. *In vivo* biosafety

Two groups of Kunming rats (total n=18) were used to evaluate the long-time cytotoxicity of the FLBS-PFH-NPs. Saline solution or FLBS-PFH-NPs solution (1 μL/g) was injected intravenously. Blood and serum samples were collected 7, 14 and 30 days after intravenous injection. Alanine aminotransferase (ALT), aspartate transaminase (AST), alkaline phosphatase (ALP), blood urea nitrogen (BUN), creatinine (Cr), lactic dehydrogenase (LDH) and creatine kinase (CK) levels were measured by the clinical laboratory of the secondary affiliated hospital of Chongqing Medical University.

2.7. Cell targeting and connection rate of FLBS-PFH-NPs to HELA cells

HeLa and normal human hepatic L02 cells in the exponential growth phase were transferred to laser confocal cell culture dishes and cultured for 24 h to form a monolayer. DMEM and RPMI 1640 cell culture medium including the FLBS-PFH-NPs (200 μL) was added to the dishes, and the cells were incubated for 2 h; next, the cell membrane was

stained with DiO. In the experiment, the same amount of non-targeted nanoparticles (NLBS-PFH-NPs) was added to the cell culture dish as a control. Then, the cells were washed three times with PBS. Finally, a confocal laser-scanning microscope (CLSM, Leica, Germany) was used to measure the targeting efficiencies of the FLBS-PFH-NPs and NLBS-PFH-NPs.

HeLa cell monolayers were detached with trypsin and prepared as uniform cell suspensions at a concentration of 2×10^5 cells/mL that were stored in sterile centrifuge tubes (200 μL per tube). Afterwards, 50 μL of the FLBS-PFH-NPs and NLBS-PFH-NPs labeled with DiI at different concentrations (0.5, 1.0, 1.5, 2.0, and 2.5 mg/mL) was added to the cell suspensions and incubated for 2 h. Next, the samples were centrifuged and washed with PBS, and the cycle was performed 3 times. Eventually, we measured the connection rates by counting the number of cells linked with red fluorescent nanoparticles using a flow cytometer.

2.8. Animal models and implantation of cervical cancer

All animals used in the experiments were purchased and bred in the Animal Center of Chongqing Medical University. All animal experiments were approved by our animal ethics committee. In addition, all the experiments and procedures were performed with the animals under complete anesthesia. All the animal experiments were conducted using protocols approved by the Institutional Animal Care and Use Committee at Chongqing Medical University. Eighteen female nude rats (4 weeks of age) were used to generate cervical cancer animal models, which were developed under sterile conditions. The nude rats were fastened to a foam sheet and disinfected with alcohol. Next, HeLa cell suspensions (1×10^7 cells/mL) with a volume of approximately 0.2 mL were injected subcutaneously. The tumor model was established after 4 weeks and measured with a caliper. The tumor volumes were calculated using the following equation: $V = 1/2 \times L \times W^2$ (W: width, L: length). The nude rats were fed until the volume of the tumor tissue was 1 cm^3.

2.9 Half circulation time and bio-distribution

To obtain the circulation time of FLBS-PFH-NPs, 0.5 mL of blood sample from New Zealand Rabbits was collected at different interval time (2 min, 5 min, 10 min, 30min, 1 h,

2h, 4h and 24h) after the injection of FLBS-PFH-NPs. The Bi concentration of each blood sample was measured using ICP after digestion using HClO4/HNO3 solution. Meanwhile, *in vivo* distribution experiment, 1mg of FLBS-PFH-NPs was injected into the tumor-bearing nude mice via tail vein. The mice were executed at 3h after administration, and the organs containing heart, liver, spleen, lung, kidney and tumor were collected and measured Bi concentrations by using ICP after digestion by HClO4/HNO3 solution.

2.10. *In vitro* and *in vivo* US imaging

Saline solution, L-PFH-NPs, NLBS-PFH-NPs and FLBS-PFH-NPs at different Bi concentrations (1.0, 2.0, 3.0, 4.0, and 5.0 mg/mL) were each placed into a self-regulating gel mold. The samples were scanned using ultrasonic diagnostic imaging equipment (Esaote Mylab 90 Type) in conventional B mode and contrast mode. US images were collected at a mechanical index of 0.6 before phase transformation was observed. High-intensity focused ultrasound (HIFU, acoustic power: 60 W, exposure duration: 2 s) was used to trigger the liquid-gas phase transition of the liposome nanoparticles. Afterwards, four groups of contrast agents separately placed into the 2 mL fractions in the EP plastic pipes. The EP plastic pipes were immersed in degassed water for HIFU exposure. Subsequently, the US images of the different agents in B and contrast mode were collected immediately before and after the phase transition. “DFY” ultrasonic quantitative analysis diagnostic system software was used to measure the acoustic intensities and gray values in the regions of interest (ROIs). An ellipse sampling frame of the DFY software was selected to be randomly placed in the ROIs of the sample US images. Then, the DFY software automatically measured the echo intensity and gray value of a selected region. After repeated measurements, the average echo intensity and gray value was determined using SPSS analysis.

New Zealand rabbits (n=20) were purchased from the Animal Center of Chongqing Medical University to perform *in vivo* US imaging experiments. All rabbits were fasted 24 h before the experiments, and their abdomens were depilated with 8% Na_2S. Then, the rabbits were intravenously anesthetized with 3% pentobarbital solution (1 mL/kg). Saline solution, L-PFH-NPs, NLBS-PFH-NPs and FLBS-PFH-NPs were injected into the four different groups of rabbits via their ear margins. The livers of the rabbits were subjected

to HIFU ablation (acoustic power: 70 W, exposure duration: 2 s) 30 s after injection. US images in B mode and contrast mode were acquired before and immediately after phase transitions. DFY Image Quantitative Analysis software was used to analyze changes in echo intensities and gray values in the ROI using the same method as described above.[9]
To demonstrate the feasibility of active targeting US imaging *in vivo*, nude mice (n=12) bearing cervical cancer were used and intravenously injection of saline solution, L-PFH-NPs, NLBS-PFH-NPs and FLBS-PFH-NPs, respectively. Then, US images of tumors were acquired before and at 3h after administration.

2.11. *In vitro* and *in vivo* CT imaging

Saline solution, L-PFH-NPs, NLBS-NPs and FLBS-PFH-NPs were used in experiments to investigate the effects of Bi_2S_3 nanoparticles on CT imaging. Simultaneously, FLBS-PFH-NPs at different Bi concentrations (1.0, 2.0, 3.0, 4.0, and 5.0 mg/mL) were employed to observe the influence of Bi_2S_3 nanoparticles on CT imaging densities. Different agents were loaded into the EP plastic pipes. CT images and the corresponding CT values in the ROI were recorded with a clinical CT scanner (GE LightSpeed, Fairfield, CT, USA) using the following parameters: tube voltage, 80 kV; tube current, 170 mA; and section thickness, 5 mm.

Normal New Zealand rabbits (n=20) of either gender, 4 months of age and a weight of 2.0 ± 0.16 kg were intravenously anesthetized with a 3% pentobarbital solution (1 mL/kg). Then, saline solution, L-PFH-NPs, NLBS-PFH-NPs and FLBS-PFH-NPs at doses of 1 mL/kg were intravenously injected. Liver CT imaging was performed before the injections and 30 min, 1 h and 2 h after injection. The CT values of liver tissues in the ROI were measured using GE ADW 4.3 software. The operating parameters were tube voltage, 80 kV; tube current, 170 mA; and section thickness, 5 mm. [48]

To demonstrate the feasibility of active targeting CT imaging *in vivo*, nude mice (n=12) bearing cervical cancer were applied and intravenously injection of saline solution, L-PFH-NPs, NLBS-PFH-NPs and FLBS-PFH-NPs, respectively. Then, CT images of tumors were acquired before and at 3h after administration.

2.12. Evaluation of *ex vivo* and *in vivo* HIFU ablation

A JC200 HIFU tumor treatment system (Chongqing HIFU Medical Technology Limited-liability Company) was used for all HIFU measurements. The focal length, diameter and operating frequency were 135 mm, 200 mm, and 0.94 MHz, respectively. A high-energy US beam was emitted from the therapeutic transducer while changes in the targeted tissue were monitored by the diagnostic transducer in real time.

Fresh bovine liver with few blood vessels and connective tissues were used for *in vitro* HIFU ablation experiments and were placed in saline solution for 30 min at 20 °C. Then, the bovine liver tissue was immersed in degassed water. Subsequently, FLBS-PFH-NPs (1 mL) were vertically injected into the liver tissue. Saline solution, L-PFH-NPs and NLBS-PFH-NPs were used as control groups. Simultaneously, HIFU was used to monitor and expose the injection areas. The HIFU ablation parameters were as follows: depth of 15 mm beneath the skin; exposure duration of 2 s; and acoustic power levels of 90, 120, 150, and 180 W. The maximum length (L, mm), width (W, mm) and depth (D, mm) of the coagulated tissues were measured after ablation, and the volume (V, mm^3) was calculated based on the following formula: $V = \pi \times L \times W \times D/6$.[49]

Tumor-bearing nude rats were used in the HIFU ablation experiment. Two weeks after tumor inoculation, female nude rats with cervical cancer (n=20) were randomly assigned to four groups and carefully anesthetized by an intraperitoneal injection of 10% chloral hydrate (60 μL/kg). Subsequently, FLBS-PFH-NPs (200 μL) were injected into the nude rats *via* the tail vein. Moreover, the same amount of saline solution, L-PFH-NPs and non-targeted NLBS-PFH-NPs was intravenously administered for comparison. After 24 h, the rats were anaesthetized and fastened to the HIFU treatment bed in the lateral position. Tumor tissues were sufficiently covered with degassed water and exposed to HIFU ablation with the following parameters: acoustic power, 120 W; exposure duration, 2 s. During HIFU treatment, hyperechoic changes in tumor tissues were imaged in real time. DFY software was used to compare the pre- and post-ablation variations by measuring the gray scale image intensities.

2.13. Histopathological analyses

The nude rats were euthanized and sacrificed the secondary day in the animal experimental center after HIFU ablation. The tumor tissues were removed and sectioned into 3 mm-thick slices. Then, representative necrotic tumor tissues were selected to perform 2,3,5-triphenyltetrazolium chloride (TTC) solution staining at 37 ℃ for 15 min. The coagulative necrosis volumes were measured according to the equation described above. Additionally, 1 cm^3 sections of tumor tissues, including the ablated tissues and the surrounding zones, were used for hematoxylin and eosin (HE) staining. Ultrastructural alterations of tumor tissues were determined using transmission electron microscopy (TEM) after fixation with glutaraldehyde. To evaluate tumor cell proliferation, immunohistochemical staining with antibodies against proliferating cell nuclear antigen (PCNA) was conducted on targeted tissues. Furthermore, TdT-mediated dUTP nick-end labeling (TUNEL) immunohistochemical examinations were also performed to obtain information on the apoptosis of the tumor tissues. PCNA-positive and TUNEL-positive cells were sorted from 6 randomly selected high-power (400× magnification) fields using an optical microscope by blind observers. The positive index (PI) and apoptosis index (AI) were expressed as the ratio of positively stained tumor cells to all cells and were estimated by counting 6 random areas at 400× magnification.

2.14. Statistical Analyses

Data were presented as the mean±standard deviation (SD). All statistical analyses were performed with SPSS software (version 21.0). Variance analyses were used to compare the differences between the experimental groups. The differences were considered to be statistically significant for $P<0.05$.

3. RESULTS AND DISCUSSION

3.1. General characterization of FLBS-PFH-NPs

The microstructure and chemical composition of FLBS-PFH-NPs were determined using different characterization techniques. The FLBS-PFH-NPs were uniform in size with a mean diameter of 458.5 nm, which was determined by dynamic light scattering

(DLS) (Figure 1a). Meanwhile, the average surface electric potential of the FLBS-PFH-NPs was measured to be – (15.5±5.8) mV (Figure 1b), which could provide guaranteed stability during circulation in the blood stream. The FLBS-PFH-NPs formed a brown suspension when diluted in double-distilled water. Imaging of the FLBS-PFH-NPs with LM and TEM showed perfect spherical morphologies with smooth surfaces and high dispersion (Figures 1d, 1f). In addition, the FLBS-PFH-NPs exhibited typical core-shell structures (the liquid core was composed of PFH, and the hydrophilic shells consisted of mixed phospholipid molecules), and Bi_2S_3 nanoparticles were randomly distributed in the lipid shell, as determined by transmission electron microscopy (TEM) (Figure 1f). To demonstrate the fluorescence imaging capabilities of the FLBS-PFH-NPs, we utilized a red fluorescent dye (DiI) during the synthesis process. Because of their lipophilic nature, the DiI molecules were incorporated into the lipid shells of the nanoparticles. The FLBS-PFH-NPs emitted fairly strong red fluorescence during fluorescence microscope observations (Figure 1e), which indicated that therapeutic agents (e.g., lipophilic anticancer drugs) could be loaded for chemotherapy using this approach. The peaks for Bi and S were detected in the EDS spectrum (Figure 1c). EDS demonstrated that the Bi_2S_3 nanoparticles were successfully inserted into the lipid droplets. As shown in supporting information Figure 2, the reflection peaks of FLBS-PFH-NPs in XRD patterns were well consistent to the Bi_2S_3 nanoparticles. Both of EDS and XRD demonstrated that the Bi_2S_3 nanoparticles have been successfully inserted into the lipid droplets. The corresponding concentrations of the Bi encapsulated in the FLBS-PFH-NPs after the addition of different volumes of Bi_2S_3 (200, 400, 600, 800, and 1000 μL), as measured by ICP-OES, were 1.0, 2.0, 3.0, 4.0, and 5.0 mg/mL, respectively. The FLBS-PFH-NPs that dispersed in water stratified into transparent and brown layers after several days; however, no obvious changes in the size and morphology of the nanoparticles occurred after gentle shaking, which indirectly confirmed their high stability. The results from these studies laid the foundation for dual-modal imaging and HIFU therapy.

3.2. *In vitro* phase transformation of FLBS-PFH-NPs

PFC-based US contrast agents have become an important research topic due to their stability, low toxicity, low viscosity and easy phase transformation.[50] PFH is a hydrophobic but highly biocompatible fluorocarbon compound with a high boiling point (≈56 °C); this makes PFH superior to the traditionally used perfluoropentane (PFP), which has a boiling point of approximately 29 °C.[44] In this study, we imaged temperature-responsive phase transformations using a fluorescence microscope after heating FLBS-PFH-NPs (Figure 2a) to investigate whether PFH could be encapsulated into FLBS-PFH-NPs and exhibit temperature-responsive behavior. No apparent changes in FLBS-PFH-NPs were observed under the microscope when the temperature of the heating plate reached 60 °C, revealing that the vaporization temperature of PFH was improved after lipid encapsulation. As expected, a series of microbubbles emerged when the temperature was raised to 64 °C. Interestingly, the number of microbubbles gradually increased at 66 °C. A temperature of 68 °C induced a subsequent increase in the size of the FLBS-PFH-NPs and generated new microbubbles, indicating that liquid PFH had been successfully encapsulated into the FLBS-PFH-NPs and displayed a perfect temperature-responsive phase-transition effect. Almost all of the microbubbles were enlarged, and the swelling of neighboring microbubbles resulted in their fusion when the temperature reached 70 °C. Finally, clusters of microbubbles started to collapse and disintegrate as the temperature continued to increase above 73 °C. This capability of US imaging and HIFU ablation is predominantly ascribed to the cavitation effect of the stable bubbles released from contrast agents.[51-52] Therefore, these *in vitro* studies confirmed the potential of FLBS-PFH-NPs for use in *in vivo* applications.

The obtained *in vitro* US imaging results were consistent with our optical microscopy observations (Figures 2b, c). The echo intensities of the FLBS-PFH-NPs in conventional B mode and contrast mode were enhanced when the HIFU acoustic power reached 60 W. Simultaneously, the intensities became more obvious when the acoustic power was increased from 60 W to 180 W (Figures $2b_2$-b_6, $2c_2$-c_6) compared to those before the phase transformations were induced (Figure $2b_1$-c_1). The presented histograms (Figures 2d-e) show the corresponding ultrasonography acoustic intensity values and gray values

before and after the phase transformations at different acoustic powers. We hypothesized that more nanoparticles occurred in the liquid-gas phase transition and formed large microbubbles when the HIFU acoustic power was gradually increased, leading to an obvious temperature increase, which could have enhanced the back scattering and increased the US intensities. Our results support this phase-transformation property and the corresponding temperature-sensitive ultrasonography behavior of FLBS-PFH-NPs. Thus, the FLBS-PFH-NPs were expected to be an agent that facilitates a phase change for stimuli-responsive ultrasonography in the *in vitro* evaporation study. We then concluded that the FLBS-PFH-NPs with PFH cores and lipid shells not only were stable at room temperature but also could transform into microbubbles, if required; therefore, PFH was used for our studies. Due to their small size, the nanoparticles could penetrate through blood vessels and target tumor tissues after folate modification. In addition, changes in temperature or HIFU irradiation induced the nanoparticles to generate micrometer-sized bubbles via a phase transformation from liquid to gas, which may have enhanced the echo intensities of the US imaging and may improve HIFU therapeutic efficiencies.

3.3. *In vitro* and *in vivo* biosafety of FLBS-PFH-NPs

We used an MTT assay and flow cytometry to evaluate the cytotoxicity of the FLBS-PFH-NPs *in vitro* against normal human hepatic L02 cells. The cell viability of L02 cells treated with FLBS-PFH-NPs at different Bi concentrations (1.0, 2.0, 3.0, 4.0, and 5.0 mg/mL) for 24 h and 48 h were measured. The MTT assay revealed that the viability of hepatic L02 cells incubated with different concentrations of FLBS-PFH-NPs was similar to that of the contrast groups cultured with PBS (Figure 3a), which was consistent with previous studies demonstrating that polymer shell-coated Bi_2S_3 nanoparticles exhibited high biocompatibility, excellent stability and desirable safety profiles.[53,69] The flow cytometry data indicated that the percentage of apoptotic cells after incubation with 5.0 mg/mL of FLBS-PFH-NPs for 24 h was approximately 7.88% (Figure 3d), which was similar to observations made for the PBS control group (Figure 3c, 7.48%). The percentage of cells that accumulated in the G1/G0 phase was 59.28% and 64.86%, respectively, following treatment with PBS and 5.0 mg/mL of FLBS-PFH-NPs

(Figures 3e-3f). No significant difference was detected between the two groups. Subsequently, we assessed the *in vivo* cytotoxicity of FLBS-PFH-NPs by measuring the physiological and biochemical indices of Kunming white rats. There were no obvious differences in the liver, kidney and heart functions before or 7, 14 or 30 days after FLBS-PFH-NP injection (Figure 3b). We concluded that the FLBS-PFH-NPs did not affect the viability of L02 cells, possessed good hemocompatibility in white rats and were therefore safe for use in biomedical applications.

3.4. *In vitro* and *in vivo* targeting efficiency of FLBS-PFH-NPs

We assessed the *in vitro* targeting efficiency of the FLBS-PFH-NPs by confocal laser scanning microscopy. As depicted in Figure 4a_1-a_2, many punctate particles emitting red fluorescence were observed around the cytoplasm of HeLa cells, which emitted green fluorescence (Figure 4a_2); fewer of these red particles were present in the non-targeted group (Figure 4a_1). Consequently, the FLBS-PFH-NPs exhibited greater cell affinity and targeting efficiency than did the NLBS-PFH-NPs. Simultaneously, few red particles were observed around the L02 cells ascribing to that most of normal human cells were negatively targeted to folic acid (Figure 4a_3-a_4). Next, we measured the targeting connection rate using flow cytometry. The connection rate gradually increased with incremental increases in the nanoparticle concentration. Additionally, this rate was clearly higher in the FLBS-PFH-NP group than in the NLBS-PFH-NP group (Figure 4b). Nanoparticles modified with folate exhibited strong interactions with the highly expressed folate receptors on tumor cells, which could have significantly improved the accumulation of nanoparticles in tumor tissues compared to the non-targeted group. Moreover, previous research has shown that folate-targeting nanoparticles can penetrate through vascular endothelial gaps and remain in tumor tissues for long periods, which demonstrates their potential for use in cancer diagnosis and agent-assisted therapy.[54-55] In conclusion, FLBS-PFH-NPs possess active and passive targeting capabilities and have the potential to accumulate in tumors and aid in cancer imaging and therapy.

3.5 Half circulation time and bio-distribution

As shown in supporting information Figure 6a, the half circulation time of

FLBS-PFH-NPs was calculated to be 2.2h. Meanwhile, the Bi distribution in tumor-bearing nude mice further demonstrated that the FLBS-PFH-NPs have been uptake by the tumor tissue in 3h after intravenous injection (supporting information Figure 6b).

3.6. *In vitro* and *in vivo* performance of US imaging

FLBS-PFH-NPs, NLBS-PFH-NPs and L-PFH-NPs displayed punctiform, tiny, and homogeneous hyperechogenicities, whereas the saline group was anechoic. The US echo intensities of the saline solution and the L-PFH-NPs were lower than those of the FLBS-PFH-NPs and NLBS-PFH-NPs (Figures $4c_1$-c_4, $4d_1$-d_4, $P<0.05$). The echo intensities were gradually enhanced with increases in the Bi_2S_3 concentrations before the phase transformation (Figures $4c_4$-c_8, $4d_4$-d_8). The line graph presented in Figure 4e shows the relationship between the acoustic intensity and the Bi_2S_3 concentration. After treatment with HIFU, the observed echo intensities of FLBS-PFH-NPs, NLBS-P FH-NPs and L-PFH-NPs were significantly higher than those observed prior to the phase transformation; no changes were observed for the control group (Figures 5a-d). We also calculated the acoustic intensity values and gray values from US imaging before and after the phase transformations (Figures 5e-f, $*P<0.05$,$**P>0.05$), which confirmed that PFH had been successfully encapsulated into the FLBS-PFH-NPs and displayed an excellent capability for transformation. Importantly, the echo intensities of FLBS-PFH-NPs and NLBS-PFH-NPs were stronger than those of L-PFH-NPs because of the encapsulation of Bi_2S_3 nanoparticles before and after the phase transformation. For US imaging, FLBS-PFH-NPs produced higher echogenicity than did the other nanoparticles, implying that the acoustic properties of microspheres could be substantially modified by utilizing specific shells.[56-57] Similarly, the introduction of Bi_2S_3 nanoparticles could change the viscoelastic properties of the lipid shells and be primarily responsible for enhancing the scattering signals of the contrast agents, which is attributed to the boosting of acoustic impedance. Raisinghani et al proposed that this type of enhancement using multiple shell structures or modifications of the shell composition altered the surface tensions of the microbubbles. [58]

We also performed US imaging on rabbit liver tissues in conventional B mode and

contrast mode before and after phase transformations to evaluate the imaging capabilities using the different contrast agents. The US imaging capabilities using the various agents were assessed by monitoring the acoustic intensity and gray value changes in the liver parenchyma. We acquired US images of the four groups (i.e., control, L-PFH-NPs, NLBS-PFH-NPs and FLBS-PFH-NPs) before and 30 s after intravenous injection. The echo intensities of the liver tissues were obviously improved in the L-PFH-NP, NLBS-NP and FLBS-PFH-NP groups when the HIFU acoustic power was 70 W. In contrast, the control group was still anechoic after HIFU irradiation (Figures 6a-d). Next, we used a DFY Ultrasonic Quantitative Analysis Diagnostic System to measure the echo intensities and gray values in the liver parenchyma (Figures 6e-f). The FLBS-PFH-NP, NLBS-PFH-NP and L-PFH-NP groups displayed higher values than those obtained prior to phase transformation (*P<0.05); no significant change was observed for the control group (**P>0.05). Notably, the echo intensities obtained from the FLBS-PFH-NP and NLBS-PFH-NP groups were higher than that of the L-PFH-NP counterpart, which may have been due to the influence of embedded Bi_2S_3 nanoparticles. Our results showed that the L-PFH-NPs, NLBS-NPs and FLBS-PFH-NPs could undergo liquid-gas phase transitions at low acoustic powers and could thus dramatically enhance the echo intensities in the liver tissue ROI, likely because the microbubbles produced backscattered signals. These results confirmed that FLBS-PFH-NPs could be used as an effective US imaging contrast agent both *in vitro* and *in vivo*.

In vivo targeting imaging, the ultrasound echo intensity in tumor tissue of folate-targeted group (supporting information Figure 3d_1-d_2, *P<0.05) was obviously higher than that in the non-targeted groups (supporting information Figure 3a-c), indicating that more active targeting FLBS-PFH-NPs were uptaken by the tumors than the non-targeting nanoparticles. This result further revealed that the accumulation in tumors is ascributing to the presence of folic acid. So, FLBS-PFH-NPs with high tumor selectivity and affinity could be used as an efficient tumor targeting agent *in vivo*.

3.7. *In vitro* and *in vivo* performance in CT imaging

We measured the CT densities for the L-PFH-NPs, NLBS-PFH-NPs and FLBS-PFH-NPs at different Bi concentrations (1.0, 2.0, 3.0, 4.0, and 5.0 mg/mL). The CT densities of both the NLBS-NP and FLBS-PFH-NP groups were higher than those of the saline and L-PFH-NP groups (Figure 7a). The CT value of the FLBS-PFH-NPs clearly increased linearly with increases in Bi_2S_3 concentration (Figure 7b).

To fully display the potential of utilizing FLBS-PFH-NPs as contrast agents for CT imaging, rabbit liver tissue was used to perform an imaging experiment. The density of the liver tissues increased with time after the administration of NLBS-PFH-NPs and FLBS-PFH-NPs. Half an hour after administration, both the NLBS-PFH-NPs and FLBS-PFH-NPs generated substantial contrast enhancement in the liver during CT imaging compared to the enhancement observed for the same nanoparticles pre-injection, and those injected with saline or L-PFH-NPs (Figures $7d_1$-g_1, d_2-g_2). No apparent change was observed in the saline and L-PFH-NP groups before and after injection (Figures 7d-e). As displayed in Figure 7c, the corresponding CT values of the NLBS-NP and FLBS-PFH-NP groups were higher than the values obtained for the same nanoparticles pre-injection and for the groups injected with saline and L-PFH-NPs. Nonetheless, no significant differences were observed in the NLBS-NPs and FLBS-PFH-NPs (Figures 7f-g). Peak enhancement was observed 1 h post-injection when the liver density increased to the maximum and the resulting images were almost saturated (Figures $7d_3$-g_3). Interestingly, the liver tissue could still be clearly identified from the surrounding tissues even after 2 h. Similarly, the CT values in the ROI obtained in the NLBS-PFH-NP and FLBS-PFH-NP groups increased markedly compared to those of previous observations and the other two groups (Figures $7d_4$-g_4). No significant differences were identified between the groups injected with L-PFH-NPs and saline in terms of the enhanced CT images and quantitative CT density values (Figure 7c). Obviously, the long circulation time of the nanoparticles in liver tissue during CT imaging was superior to that of commonly used clinical CT contrast agents, showing the potential for our FLBS-PFH-NPs to improve the detection of hepatic metastases. Moreover, previous research indicated that a prolonged circulation time and high contrast densities could lead to CT contrast agents with superior performance in vascular imaging, tumor angiogenesis

imaging, and multivalent targeted imaging agents for selective detection. Furthermore, similar results have been previously reported and showed that Bi_2S_3 nanoparticles could act as CT contrast agents *in vivo*.[22,59-62]

In vivo tumor-targeted CT imaging，as shown in supporting information Figures 4a-b, the tumors from the targeted group could be readily recognized in CT images, in contrast to the non-enhanced tumors from the non-targeted group. The CT value of tumor in the targeted group was obviously enhanced than that in the non-targeted groups (supporting information Figure 4c,*P<0.05).Besides, we observed that the vascular CT contrast of mice was enhanced than pre-injection(supporting information Figures 5, *P<0.05).

3.8. *Ex vivo* and *in vivo* evaluation of HIFU ablation

The entire ablation process was performed on degassed bovine livers *in vitro*, and the process was monitored by real-time US imaging in B-mode based on changes in the relevant quantitative coagulative necrosis volumes (Figure 8a), gray scale values (Figure 8b) and acoustic intensities (Figure 8c) at the focus. Treatment for the same amounts of time and HIFU acoustic power (90 W/cm^2, 120 W/cm^2, 150 W/cm^2 and 180 W/cm^2) showed that the mean coagulative necrosis volumes of liver tissues caused by HIFU in the groups that received the FLBS-PFH-NP and NLBS-PFH-NP treatments were higher than the volumes in the groups that received saline and L-PFH-NP (*P<0.05, **P<0.05). Moreover, the ablated volume of bovine liver after L-PFH-NP injection was larger than that observed for the group injected with saline. In contrast, no obvious differences were observed in tissues treated with the FLBS-PFH-NPs and NLBS-PFH-NPs under the same conditions (#P>0.05). The US images and macroscopic coagulative necrosis before and after HIFU exposure at 150 W for 2 s are shown in the Supplementary information (Figures S1a-e). In addition, the corresponding gray values and acoustic intensities indicated significant changes for the groups injected with FLBS-PFH-NPs, NLBS-PFH-NPs and L-PFH-NPs after HIFU exposure; these values were higher for the groups injected with FLBS-PFH-NPs and NLBS-PFH-NPs than those observed for the group injected with L-PFH-NPs (*P<0.05, **P<0.05). Concurrently, an increasing trend was found with regards to the coagulative necrosis volumes, gray values and acoustic intensities when the HIFU acoustic power and irradiation times were gradually increased.

This phenomenon was attributed to the dependency of enhanced ultrasonic absorption on Bi_2S_3 nanoparticles, which changed the acoustic impedance in tissues and intensified the cavitation effect that was induced by the phase transformation of PFH. Therefore, FLBS-PFH-NPs show promise as HIFU synergistic agents.

We further investigated the synergistic effects of FLBS-PFH-NPs for HIFU ablation on the *in vivo* ablation of cervical cancer in mice. The tumor tissues were exposed to HIFU after an intravenous administration of different agents (Figure 8d). After HIFU irradiation, variations in the acoustic signals of the different groups were immediately observed. When saline solution was injected, no obvious changes in the gray scale were detected. Noticeably, the gray scale change was higher in the folate-targeted group than that in the other three non-targeted groups (Figure 8f). Afterwards, we removed the tumor tissues from the nude rats to perform TTC staining and measure the ablation volumes (Figure 8e). A sharply demarcated region between the necrotic (white) and non-ablated tissues (red) was observed upon gross inspection (Figure 9a). This result suggested the ability of the nanoparticles to destroy malignant lesions without damaging the surrounding normal tissues. The coagulative necrosis volumes of the tumor tissues in the folate-targeted group were substantially larger than those in the groups injected with saline, L-PFH-NPs and NLBS-PFH-NPs under the same irradiation conditions (Figures 8h, 9a, $^*P<0.05$), consistent with the US imaging results (Figures 8d-g). This finding further demonstrated that FLBS-PFH-NPs could enhance the synergistic therapeutic effects of HIFU ablation cancer surgery at low power levels.

Microscopy examination of the tumors revealed varying degrees of destruction in the exposed regions. There was no distinct coagulative necrosis of the tumor tissues in the saline group after HE staining (Figure $9b_1$). In contrast, sharp demarcation lines representing variations in the cell injury layers between the necrotic and non-necrotic regions were observed in the other three groups. The coagulated necrotic tissue exhibited the typical damage consisting of lysed cell membranes and nuclear fragments, which were accompanied by a considerable amount of evenly stained red substances (Figures $9b_2$- b_4). In comparison, fewer cells with blue nuclear staining were observed in the folate-targeted group (Figure $9b_4$) than in the groups treated with the L-PFH-NPs and NLBS-PFH-NPs

(Figures $9b_2$-b_3), implying that the FLBS-PFH-NPs could damage tumor cells and led to more efficient HIFU ablation. Ultrastructural examinations reconfirmed the irreversible cellular damage in the targeted regions, as observed by TEM (Figure 9c). In the saline-treated group, the cells were still structurally intact, and chromatin occasionally condensed in a few cells (Figure $9c_1$). However, in the folate-targeted group (Figure $9c_4$), the cell and nuclear membranes ruptured, and the nuclei and organelles disappeared. Compared with the two other non-targeted groups (Figures $9c_2$-c_3, L-PFH-NPs and NLBS-PFH-NPs), the cell morphologies were still intact, but there was a mass of interrupted or undefined cellular and nuclear membranes, as well as a number of damaged organelles.

We assessed the HIFU ablation effects of the FLBS-PFH-NPs against cervical tumors in nude rats using histological and immunohistochemical methods. Immunohistochemical staining with antibodies against proliferating cell nuclear antigen (PCNA) was conducted to evaluate the cell proliferation. PCNA expression was visualized as brown granules in cell nuclei and was observed for all the experimental groups. PCNA staining was reduced in the coagulation necrosis region after HIFU ablation, while it was positive in the surrounding region of normal tissue. Additionally, the positive index (PI) of PCNA in the folate-targeted group was lower than that of the other three non-targeted groups (Figures 9e, 8g; *$P<0.05$). The cell apoptosis in tissue sections after HIFU ablation was assessed using a TUNEL assay. We detected apoptotic cells in the surrounding areas of the necrotic region in all the groups, which was in agreement with the observations from the proliferation assay (Figure 9d). We concluded that the apoptotic index (AI) was higher in the folate-targeted group than in the other three non-targeted groups (Figure 8 h, *$P<0.05$). In short, all these results demonstrated that the HIFU ablation efficiency of the folate-targeted group was significantly higher than those of the non-targeted groups.

It is well known that HIFU mainly occurs through thermal cavitation effects. Thermal ablation therapy is able to destroy target tissues by localized deposition of thermal energy, which rapidly increases the tissue temperature (by more than 60 °C) and can stimulate

protein denaturation and coagulation necrosis. In addition, the cavitation effect of HIFU therapy can also change the function and structure of cell membranes to kill tumor cells using the resulting shock waves and the jet flow produced by acoustic cavitation. Furthermore, several other factors also facilitate HIFU ablation, such as mechanical effects, acoustic streaming and shear stress, which are strongly dependent on the generation of microbubbles. However, the US energy will attenuate as it is transmitted through biological tissues, which would reduce the deposition of US energy and reduce the HIFU ablation efficiency. Thus, there is an urgent need to introduce a synergistic contrast agent to improve therapeutic efficiencies.

Because of the size of nanoparticles, the permeability and retention (EPR) effect is improved by the leaky vasculature and poor lymphatic drainage in tumor tissues, [63-64] which results in the continuous accumulation of nanoparticles from the blood circulation system.[65] HIFU exposure would also induce transient permeability of cell membranes that could enhance the EPR effect. Importantly, the accumulation of nanoparticles in tumor tissues would increase as a result of folate-targeted modifications,[32] which could produce microbubbles and result in HIFU synergistic effects.[66] The FLBS-PFH-NPs could serve as a phase change agent and form microbubbles in targeted regions upon HIFU irradiation, which could enhance the cavitation effect and thus improve the US energy deposition in targeted regions.[67-68] Moreover, the introduction of encapsulated Bi_2S_3 nanoparticles could possibly alter the acoustic environments to enhance the absorption of US energy, which could further improve the therapeutic efficiency of HIFU by increasing thermal effects.[69] More importantly, Bi_2S_3 nanoparticles could act as potential extrinsic cavitation nuclei and could lower the cavitation threshold, which would be beneficial for improving the cavitation effect of HIFU. Finally, FLBS-PFH-NPs would produce a concussion and crush injury under the effect of US waves and could cause mechanical damage to tissues. The multifold mechanisms mentioned above are exhibited by FLBS-PFH-NPs and could exert synergistic effects for HIFU ablation.

Nonetheless, several limitations of our study must be addressed. We analyzed the thermal and cavitation effects caused by FLBS-PFH-NPs. However, our experimental set up did not account for the standardization of therapy responses and stabilities or the activity of the FLBS-PFH-NPs under biologically relevant conditions.

We believe that the nanoparticles we developed have the potential for use in biomedical applications because of the low dose requirements of the contrast agents and their mild therapeutic powers; thus, these particles not only meet the demands for notably improving therapeutic efficiencies but are also safe for clinical applications. Because of all these factors, FLBS-PFH-NPs could serve as synergistic agents to increase HIFU ablation efficiencies at low power settings and to shorten exposure times.

4. CONCLUSIONS

In summary, we successfully prepared novel folate-targeted liposome-encapsulated Bi_2S_3 and PFH nanoparticles, FLBS-PFH-NPs, which are promising materials for clinical diagnostic applications. PFH equipped with temperature-responsive phase-transformation properties could improve the imaging resolution, the HIFU therapeutic effects, and the penetration of micro-sized bubbles in target tissues. Moreover, the encapsulated Bi_2S_3 nanoparticles endowed the FLBS-PFH-NPs with the ability to enhance CT imaging and HIFU therapeutic efficiencies. Based on our experiments, we conclude that FLBS-PFH-NPs can improve US and CT dual-modal imaging techniques and the synergistic therapeutic efficiency of HIFU ablation. Therefore, future research should be dedicated toward the development of multifunctional and multimodal theranostic agents for use in cancer therapy.

ACKNOWLEDGMENTS

This work was supported by the National Nature Science of China (Grant No. 81227801, 81130025, 81401423，51402329, 81501484). We are thankful to Shuai Wei for his help in CT imaging technical support Besides,we are thankful to Qi Wang for his help in HIFU technical support.

REFERENCES

1. Liu Z，Lammers T， Ehling J， Fokong S, Bornemann J，Kiessling F， Gätjens J. Biomaterials. 2011;32:6155-63.

2. Ren L, Chen S,Li H,Zhang Z, Ye C, Liu M, Zhou X. Nanoscale. 2015; 7 :12843-50.

3. Yan Lin, Zhi-Yi Chen, Feng Yang. Current Pharmaceutical Design. 2013; 19: 3342-3351.

4. Louie A. Chem Rev.2010; 110:3146-95.

5. A. Novell J, M Escoffre, A Bouakaz. Curr. Mol. Imaging. 2013; 2:77–88.

6. Lee N, Cho HR, Oh MH, Lee SH, Kim K, Kin BH, Shin K, Ahn TY, Choi JW, Kim YW, Choi SH, HyeonT. *J* Am Chem Soc .2012;134:10309-12.

7. Barrefelt AA,BrismarTB, Egri G, Aspelin P, Olsson A, Oddo L, Margheritelli S, Caidahl K, Paradossi G, Dähne L, Axelsson R, Hassan M. EJNMMI Res.2013;3:12.

8. Brismar TB, Grishenkov D, Gustafsson B, Härmark J, Barrefelt A,Kothapalli SV, Margheritelli S, Oddo L,Caidahl K, Hebert H, Paradossi G. Biomacromolecules. 2012;13:1390-9.

9. Teraphongphom N, Chhour P2, Eisenbrey JR, Naha PC, Witschey WR, Opasanont B, Jablonowski L, Cormode DP, Wheatley MA. Langmuir. 2015;31:11858-67.

10. Huynh E, Lovell JF, Helfield BL, Jeon M, Kim C, Goertz DE, Wilson BC, Zheng G. J Am Chem Soc.2012;134:16464-7.

11.Kang E,Min HS, Lee J, Han MH,Ahn HJ, Yoon IC, Choi K,Kim K, Park K, Kwon IC. Angew. Chem. Int. Ed. 2010; 49:524-8.

12.Chen Y,Yin Q,Ji X, Zhang S, Chen H,Zheng Y, Sun Y, Qu H,Wang Z, Li Y, Wang X, Zhang K, Zhang L, Shi J. Biomaterials**.** 2012**;***33:*7126-37.

13. Ao M, Wang Z, Ran H, Guo D, Yu J, Li A, Chen W, Wu W, Zheng Y. J Biomed Mater Res B Appl Biomater. 2010 ;93:551-6.

14. Barnett BP, Ruiz-Cabello J, Hota P, Ouwerkerk R, Shamblott M J, Lauzon C, Walczak P, Gilson WD, Chacko VP Kraitchman D L, Arepally A, Bulte J W. Contrast Media Mol Imaging . 2011;6: 251–9.

15.Ke, H.; Yue, X.; Wang, J.; Xing, S.; Zhang, Q.; Dai, Z.; Tian, J.;Wang, S.;Jin, Y. Small. 2014;10: 1220-7.

16. Mousnier L, Huang N, Morvan E, Fattal E, Tsapis N. Int J Pharm.2014; 471:10-7.

17.Sun Y, Wang YJ, Niu CC, Eric M Strohm, Zheng YY, Ran HT, Huang RZ, Zhou D, Gong YP, Wang ZG, Wang D, Michael C Kolios. Adv. Funct. Mater. 2014; 24, 7674-80.

18.Haller C, Hizoh I. Invest Radio.2004;39:149-54.

19.Rabin O, Manuel Perez J, Grimm J, Wojtkiewicz G, Weissleder R. Nature materials. 2006;5:118-22.

20.Kinsella JM, Jimenez RE, Karmali PP. Angew Chem Int Ed Engl. 2011;50:12308-11.

21.Ai K, Liu Y, Liu J, Yuan Q, He Y, Lu L. Adv. Mater. 2011;23:4886-91.

22.Xu C, Tung GA, Sun S. Chem. Mater. 2008;20:4167-9.

23.Zheng X, Shi J, Bu Y, Tian G, Zhang X, Yin W, Gao B, Yang Z, Hu Z, Liu X, Yan L, Gu Z, ZhaoY. Nanoscale 2015;7:12581-91.

24.Yousefi M , Sabet M, Salavati-Niasari M, Hamid Emadi. Journal of Cluster Science. 2012; 23:511-25.

25.Brown AL1, Naha PC2, Benavides-Montes V1, Litt HI3, Goforth AM1, Cormode DP4. Chem Mater. 2014;26:2266-2274.

26.Waggoner SE. Lancet. 2003;361:2217-25.

27.Wang JQ, Wang T, Shi F, Yang YY, Su J, Chai YL, Liu ZA. Asian Pac J Cancer Prev.2015;16:5957-61.

28.Lee DE, Koo H, Sun IC, Ryu JH, Kim K, Kwon IC. Chem Soc Rev.2012;41:2656-72.

29.Caldorera-Moore ME, Liechty WB, Peppas NA. Acc Chem Res.2011;44:1061-70.

30.Zhu J, Zhu H, Mei Z, Zhang L, Jin C, Ran L, Zhou K, Yang W. Br J Radiol.2014;87:20140374.

31.Hoogenboom M, Eikelenboom D, den Brok MH, Heerschap A, Futterer JJ, Adema GJ. Ultrasound Med Biol. 2015;41:1500-17.

32.Orgera G, Monfardini L, Della Vigna P, Zhang L, Bonomo G, Arnone P. Radiol Med. 2011;116:734-48.

33.Sun Y, Zheng Y, Ran H, Zhou Y,ShenH,ChenY,Chen H, Krupka TM, Li A,Li P, Wang Z. Biomaterials .2012;33:5854-64.

34. Jaiswal P, Gidwani B, Vyas A. Artif Cells Nanomed Biotechol .2014.

35. Low PS, Henne WA, Doorneweerd DD. Acc Chem Res. 2008;41:120-9.

36. Vergote I, Leamon CP. *Ther* Adv Med Oncol. 2015;7:206-18.

37. Barar J, Kafil V, Majd MH, Barzegari A, Khani S,Johari-Ahar M,Asgari D, Cokous G, Omidi Y. J Nanobiotechnology. 2015;13:26.

38. Masoud Salavati-Niasari Zeynab Behfard, Omid Amiri Elahe Khosravifard,S Mostafa Hosseinpour-Mashkani. J Clust Sci .2013;24:349–363.

39. Masoud Salavati-Niasari, Zeynab Behfard, Mahnaz Maddahfar. Journal of Industrial and Engineering

Chemistry. 2014; 20:4066–4075

40. D Ghanbari, M Salavati-Niasari, S Karimzadeh, S Gholamrezaei. Journal of NanoStructures. 2014; 4: 227-232.

41. Masoud Salavati-Niasari,Davood Ghanbari,Fatemeh Davar. Journal of Alloys and Compounds. 2009; 488:442-447.

42. Masoud Salavati-Niasari, Zeynab Behfard. Asia-Pacific Journal of Chemical Engineering.2014; 9: 16–23.

43. Qazvini NT, Zinatloo S. J Mater Sci: Mater Med .2011;22:63–69.

44. Hao Y, Guo L, Abudula A, Saidoula W, Guo X. Int J Clin Exp Med.2014;7:5330-5.

45.Naha PC1, Davoren M, Lyng FM, Byrne HJ. Toxicol Appl Pharmacol. 2010;246:91-9.

46.Maher MA1, Naha PC2, Mukherjee SP2, Byrne HJ2. Toxicol In Vitro. 2014;28:1449-60.

47.Naha PC1, Byrne HJ. Aquat Toxicol. 2013;132-133:61-72.

48.Cormode DP1, Naha PC, Fayad ZA. Contrast Media Mol Imaging. 2014;9:37-52.

49.Peek MC, Ahmed M, Napoli A, et al. The British journal of surgery. 2015;102:873-82.

50. Diaz-Lopez R, Tsapis N, Fattal E. Pharmaceutical research. 2010;27:1-16.

51. Kopechek JA, Park EJ, Zhang YZ, Vykhodtseva NI, McDannold NJ, Porter TM. Physics in medicine and biology. 2014;59:3465-81.

52. Hoang NH, Murad HY, Ratnayaka SH, Chen C, Khismatullin DB. Ultrasound Med Biol. **2014**;40: 1869-81.

53.Fang Y, Peng C, Guo R, et al. Analyst. 2013;138:3172-80.

54. Zwicke GL, Mansoori GA, Jeffery CJ. Nano Rev. **2012,** *3,* 1.

55. Xing W, Zhigang W, Bing H, et al. J. Ultrasound Med. 2010;29:609-14.

56. Guedra M, Valier-Brasier T, Conoir JM, Coulouvrat F, Astafyeva K, Thomas JL. The Journal of the Acoustical Society of America .2014;135:1044-55.

57.Stride E. Philosophical transactions Series A, Mathematical, physical, and engineering sciences .2008;366:2103-15.

58 Raisinghani A, DeMaria AN. The American journal of cardiology. 2002;90:3j-7j.

59. Sun H, Yuan Q, Zhang B, Ai K, Zhang P, Lu L. Nanoscale. 2011;3:1990-6.

60. Oh MH, Lee N, Kim H, et al. Journal of the American Chemical Society. 2011;133:5508-15.

61. EckW, Nicholson AI, Zentgraf H, Semmler W, Bartling S. Nano Lett.**2010;**10:2318-22.

62. Pan D, Roessl E, Schlomka JP, et al. Angewandte Chemie (International ed in English). 2010;49:9635-9.

63.Danhier F, Feron O, Préat V. J.Control. Release.2010:148:135–146.

64.Iyer AK, Khaled G, Fang J, Maeda H. Drug Discovery Today. 2006; 11: 812.

65. Oeffinger BE, Wheatley MA. Ultrasonics.2004;42:343-7 .

66. Chung MF, Chen K J, Liang H F, Liao ZX, Chia WT, Xia Y, Sung HW. Angew. Chem. Int. Ed.2012;51:10089-93.

67. Chen Y, Chen H, Sun Y, Zheng Y Y, Zeng D P, Li FQ, Zhang SJ, Wang X, Zhang K, Ma M, He QJ, Zhang L, Shi L. Angew. Chem. Int. Ed.2011;50: 12505-9.

68. Wang X, Chen H, Chen Y, Ma M, Zhang K, Li F, Zheng Y, Zeng D, Wang Q, Shi J. Adv. Mater.2012;24:785-91.

69. Yao M H, Ma M, Chen Y, Jia XQ, Xu G, Xu HX, Chen HR, Wu R. Biomaterials. 2014; 35:8197-205.

Figure Legends

Scheme 1. Schematic illustration of the microstructure of FLBS-PFH-NPs and the phase-transformation process by means of heating or ultrasound irradiation.Meanwhile, a schematic of HIFU ablation principles.

Figure 1. (a-b) Particle size and potential distribution images of FLBS-PFH-NPs were detected by dynamic light scattering measurement. **(c)** EDS spectrum of FLBS-PFH-NPs. **(d-e)** Bright field optical microscopy image(at ×1000 magnification) and inverted fluorescence microscope image of FLBS-PFH-NPs. **(f)**TEM images of prepared FLBS-PFH-NPs. Particles were highly dispersed and spherical. Black particles were Bi_2S_3 particles and present on the shell of lipid microsphere.

Figure 2. (a) Optical microscopic images of FLBS-PFH-NPs after heating-induced phase transformation (a_1 60^0C; a_2 64^0 C; a_3 66^0 C; a_4: 68^0 C; a_5: 70^0 C; a_6: 73^0 C). **(b-c)** US images of FLBS-PFH-NPs in B mode and contrast mode before and after phase transformation at different HIFU acoustic power (b_1,c_1:before,0w; b_2,c_2: 60w,2s; b_3,c_3: 90w,2s; b_4,c_4:120w,2s; b_5,c_5:150w,2s; b_6,c_6:180w,2s). **(d-e)** ultrasound acoustic intensity and gray value before and after phase transformation at different HIFU acoustic power.

Figure 3. Cytotoxicity effect of FLBS-PFH-NPs on normal human hepatic L02 cell *in vitro* and *in vivo*. **(a)** Cell viability of L02 cells treated with FLBS-PFH-NPs at different Bi concentrations (1.0, 2.0, 3.0, 4.0, 5.0mg/mL) for 24h and 48h. **(b-c)** Cell apoptosis of L02 cell treated with FLBS-PFH-NPs at 5.0mg/mL Bi concentration for 24h. **(d-e)**: Cell cycle of L02 cell treated with FLBS-PFH-NPs at 5.0mg/mL for 24h. **(f)**Long-time cytotoxicity was evaluated by the biochemical and blood parameters.

Figure 4.(a) Confocal laser scanning microscope images of contrast agents targeted to HeLa cells and normal human L02 hepatic cells(a_1,a_3:NLBS-PFH-NPs; a_2,a_4: FLBS-PFH-NPs). **(b)** Connection rate of contrast agents targeted to HeLa cells. **(c-d)** *In vitro* ultrasound images of different contrast agents in B mode and contrast mode before phase transformation (c_1,d_1: Saline solution ; c_2,d_2:L-PFH-NPs; c_3,d_3: NLBS-PFH-NPs ; c_4-c_8,d_4-d_8: FLBS-PFH-NPs at different Bi concentrations(1.0, 2.0, 3.0, 4.0, 5.0mg/mL mg/ml). **(e)** Ultrasound acoustic

intensity of FLBS-PFH-NPs at different Bi concentrations (1.0, 2.0, 3.0, 4.0, 5.0mg/mL mg/ml) before phase transformation.

Figure 5. (a-d) B-mode and contrast mode ultrasound images of different contrast agents (a_1-d_1: saline solution; a_2-d_2:L-PFH-NPs; a_3-d_3: NLBS-PFH-NPs; a_4-d_4: FLBS-PFH-NPs)before (a_1-a_4, c_1-c_4) and after (b_1-b_4,d_1-d_4) phase transformation at the same HIFU acoustic power (at 60w for 2s). **(e-f)** ultrasound acoustic intensity and gray value before and after phase transformation of different contrast agents (**P*<0.05,***P*>0.05)

Figure 6.(a-d) In vivo ultrasound images of rabbits' liver tissue in B mode and contrast mode before (a_1, b_1, c_1 d_1 :B mode; a_3, b_3, c_3 d_3: contrast mode) and after (a_2, b_2, c_2 d_2:B mode; a_4, b_4, c_4 d_4: contrast mode) phase transformation at the same HIFU acoustic power (at 70w for 2s) (a: saline solution; b: L-PFH-NPs; c: NLBS-PFH-NPs; d: FLBS-PFH-NPs). **(e-f)** Ultrasound echo intensity and gray value of liver tissue in rabbits before (purple bars) and after (red bars) phase transformation (***P*>0.05;**P*<0.05).

Figure 7.(a) CT images of different agents *in vitro* (a_1:saline solution; a_2: L-PFH-NPs; a_3: NLBS-PFH-NPs; a_4: FLBS-PFH-NPs at different Bi concentrations (1.0, 2.0, 3.0, 4.0, 5.0mg/mL mg/ml). **(b)** CT value of FLBS-PFH-NPs at different Bi concentrations (1.0, 2.0, 3.0, 4.0, 5.0mg/mL mg/ml) *in vitro*. **(c)**The computed tomography (CT) value of the liver in rabbits before and at 30 min, 1h and 2 h) after injection of different agents, respectively (saline solution, L-PFH-NPs, NLBS-PFH-NPs, FLBS-PFH-NPs). **(d-g)** CT imaging of rabbit liver tissues before (d_1-g_1) and at 30min (d_2-g_2), 1h (d_3-g_3) and 2 h (d_4-g_4) after injection of different agents (a: saline solution; b: L-PFH-NPs; c: NLBS-PFH-NPs; d: FLBS-PFH-NPs).

Figure 8. (a-c) Quantitative analysis of HIFU therapeutic efficacies in vitro after administration of different agents with (f: coagulative volume; g: gray value; h: acoustic intensity; **P*<0.05,***P*<0.05,# *P*>0.05) **(d-g)** Typical *in vivo* B-mode ultrasound images before (a_1-d_1) and after (a_2-d_2) HIFU exposure on cervical cancer in rude rats after injecting different agents (a:saline solution; b:L-PFH-NPs; c:NLBS-PFH-NPs; d:FLBS-PFH-NPs). **(h-i)** Quantitative analysis of HIFU therapeutic efficacies in vivo after administration of different agents (e: coagulative volume; f gray value; **P*<0.05). **(j-k)** PCNA PI and apoptosis index (AI) of TUNEL in different groups after HIFU ablation (*P < 0.05).

Figure 9.(a) Macroscopic inspections of cervical cancer exposed to HIFU after TTC staining. The necrotic tissues are represented in gray, non-ablated tumors in red (a_1:saline solution; a_2:L-PFH-NPs; a_3:NLBS-PFH-NPs; a_4:FLBS-PFH-NPs). **(b)** HE staining of the tumor tissue after HIFU ablation. There exists a significant boundary between the ablated and non ablated region (200×magnification). (b_1:saline solution; b_2:L-PFH-NPs; b_3:NLBS-PFH-NPs; b_4:FLBS-PFH-NPs). **(c)** TEM images of tumor tissues after HIFU ablation. (c_1:saline solution ; c_2:L-PFH-NPs; c_3:NLBS-PFH-NPs; c_4:FLBS-PFH-NPs).**(d)** expression of TUNEL in tumor tissue by immunohistochemical examination.TUNNEL-positve cells are in brown , negative ones in blue (d_1:saline solution; d_2:L-PFH-NPs; d_3:NLBS-PFH-NPs; d_4:FLBS-PFH-NPs). **(e)** Histochemical analysis of PCNA expression after HUIFU in tumor tissue. PCNA-positive cell are represented in brown, negatives in blue (e_1:saline solution ; e_2:L-PFH-NPs; e_3:NLBS-PFH-NPs; e_4:FLBS-PFH-NPs).

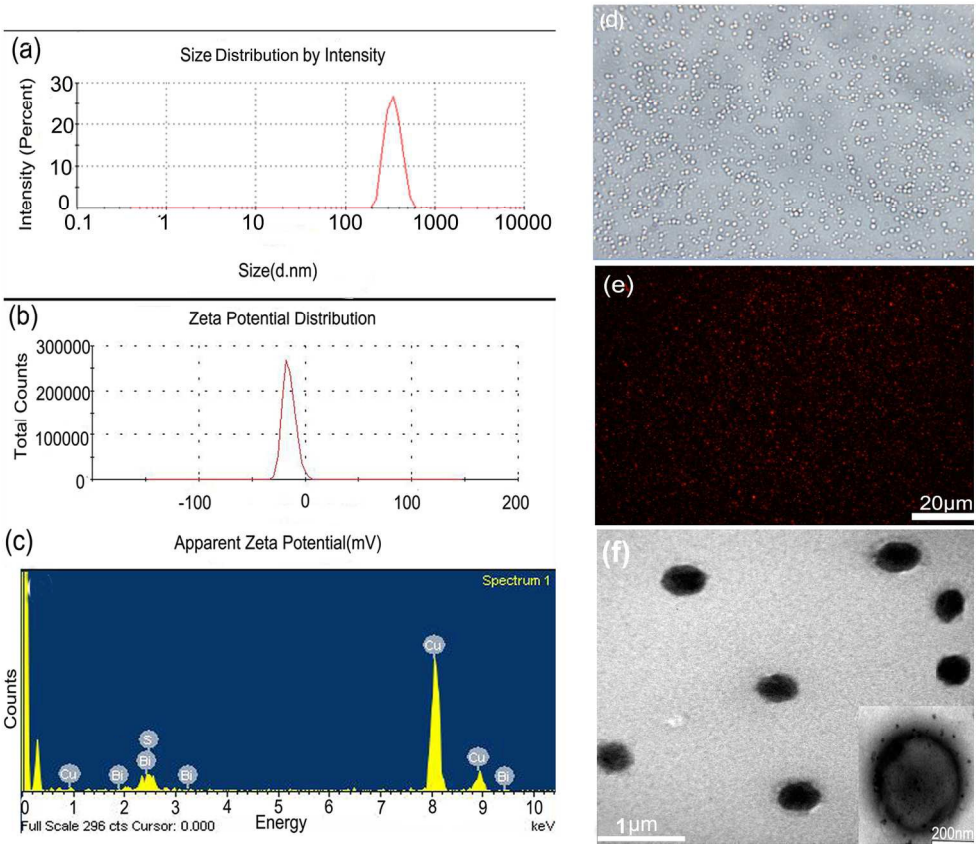

242x205mm (300 x 300 DPI)

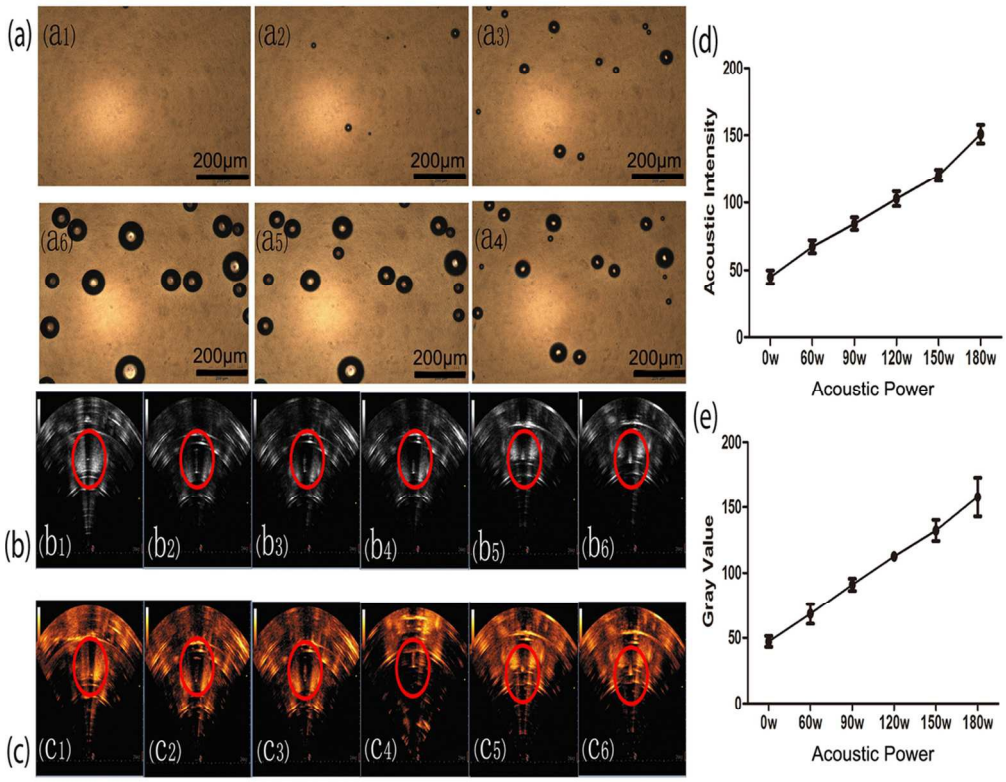

102x86mm (300 x 300 DPI)

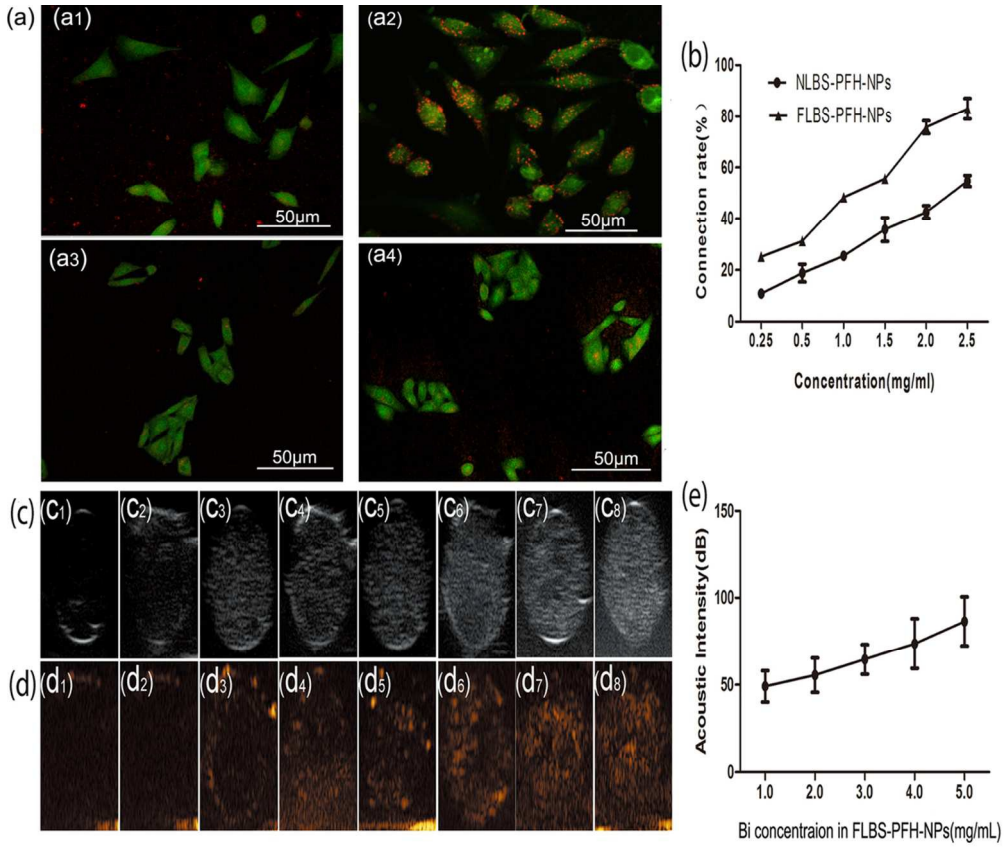

102x88mm (300 x 300 DPI)

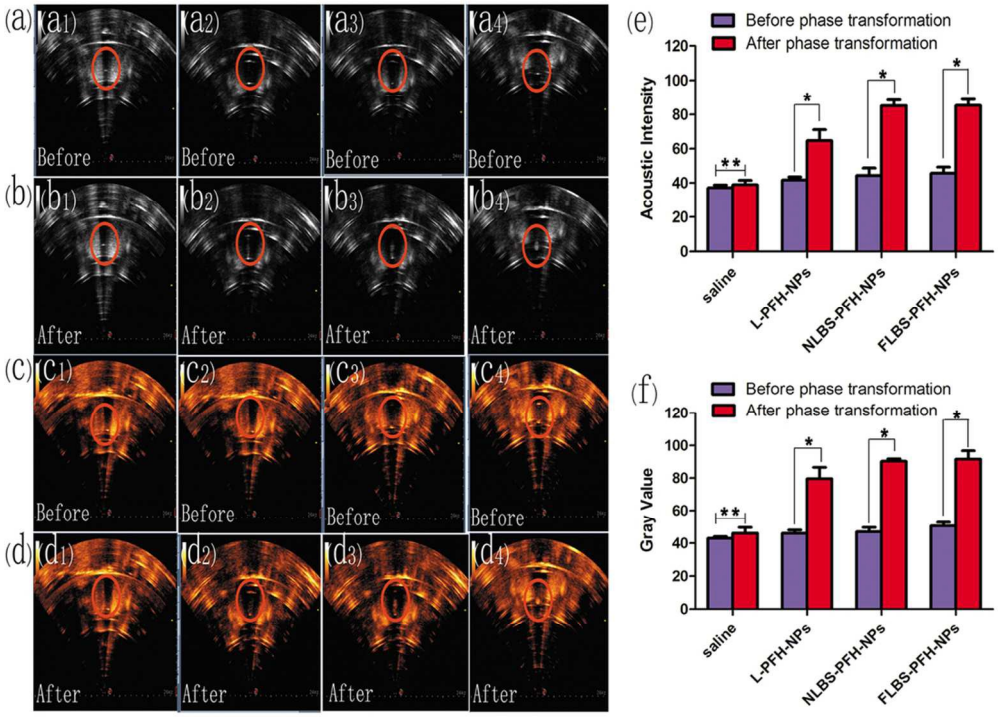

93x68mm (300 x 300 DPI)

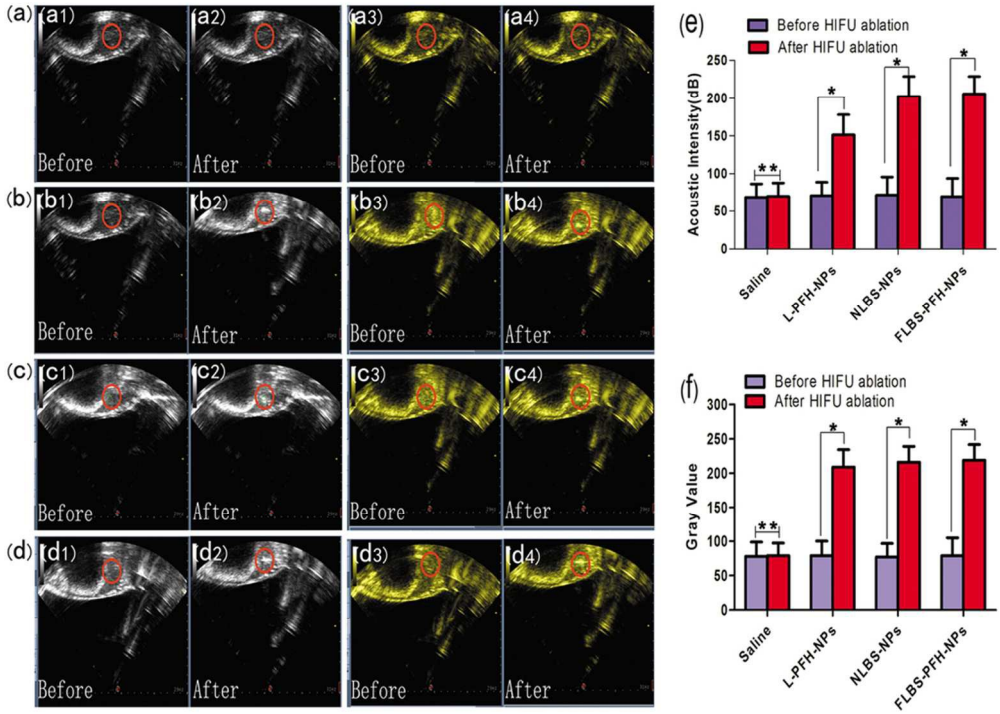

86x63mm (300 x 300 DPI)

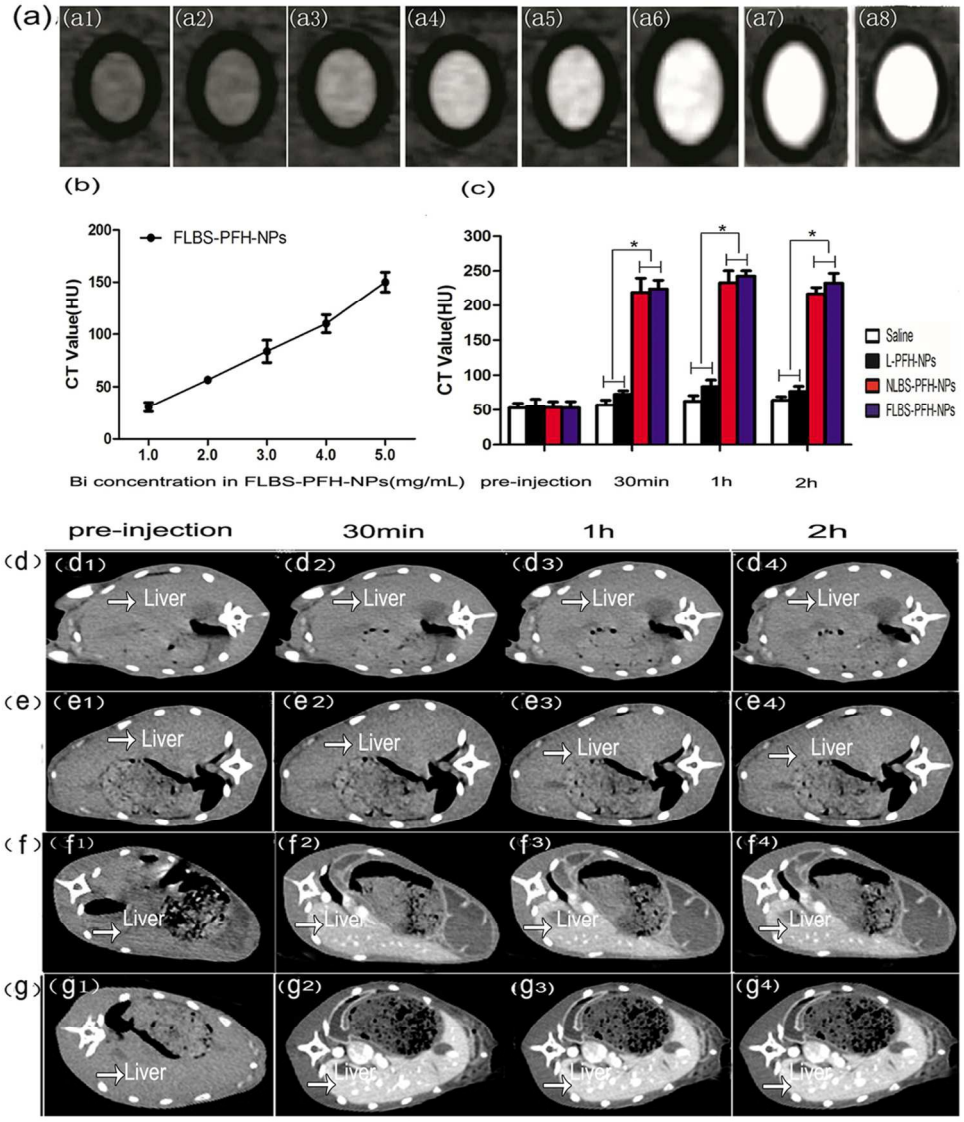

102x116mm (300 x 300 DPI)

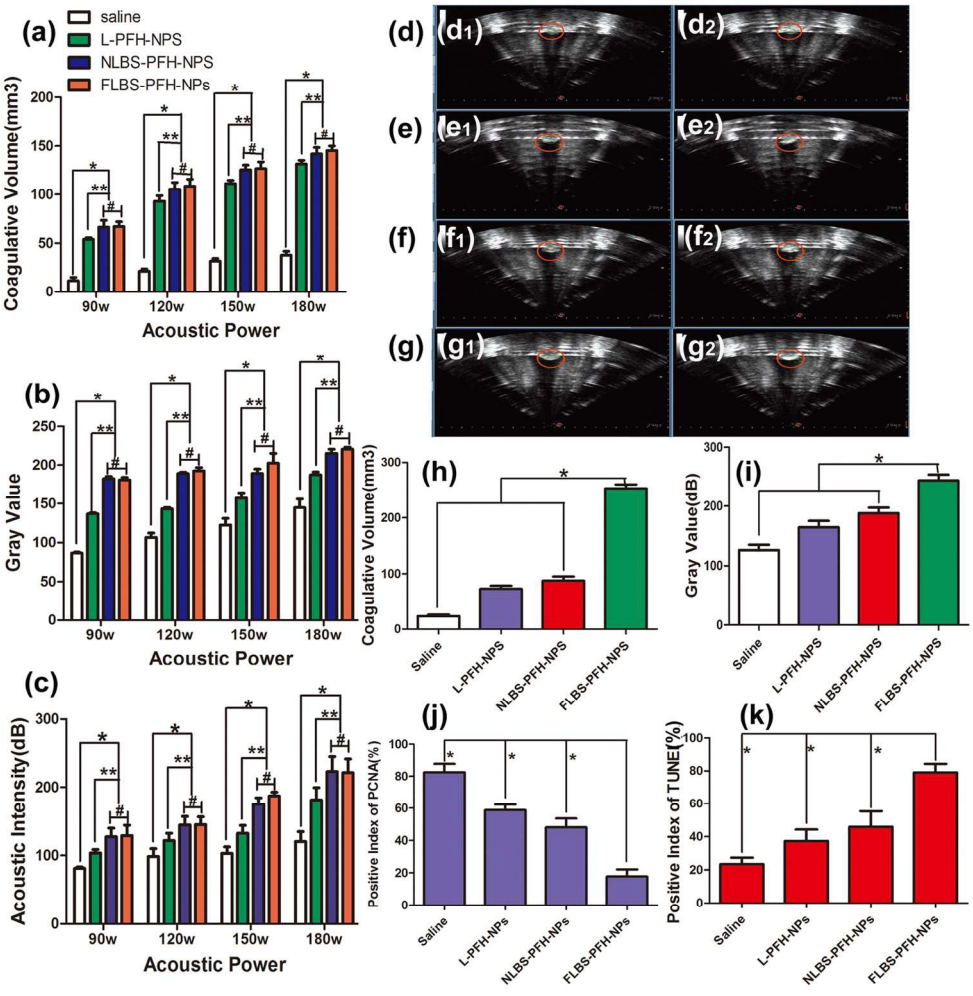

140x143mm (300 x 300 DPI)

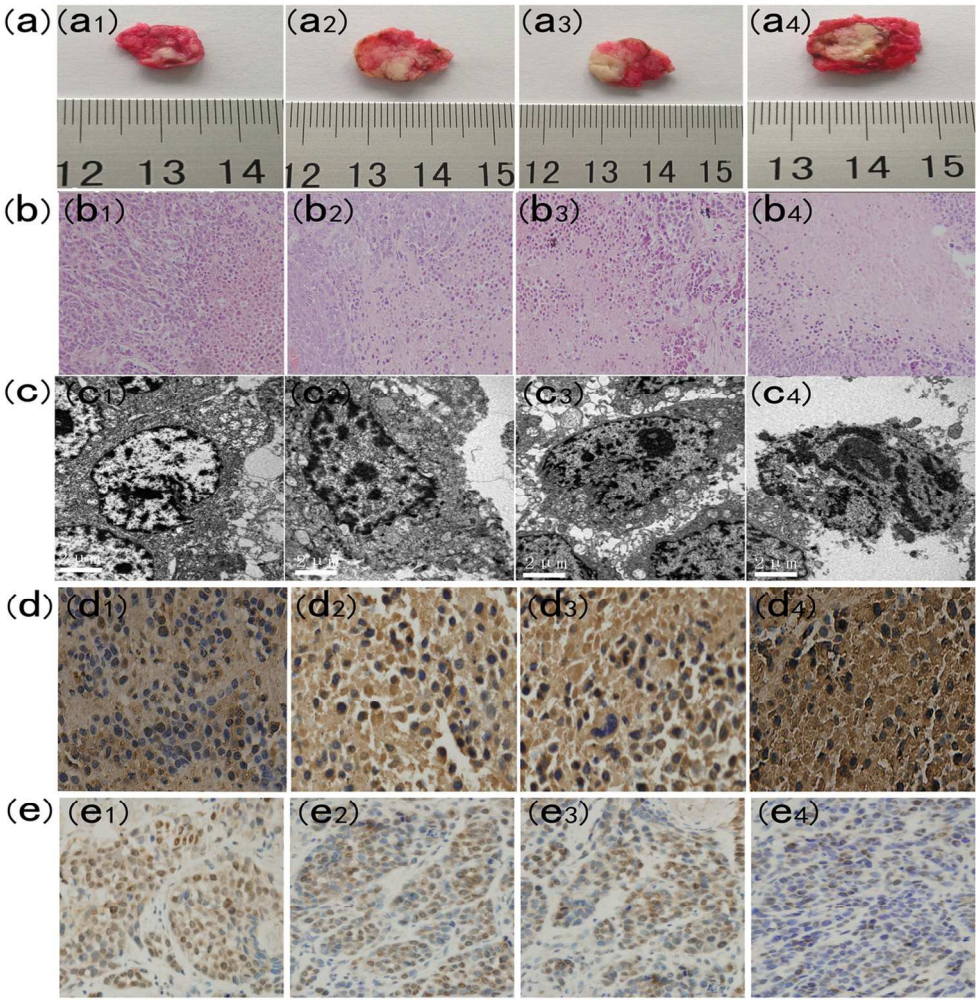

129x131mm (300 x 300 DPI)

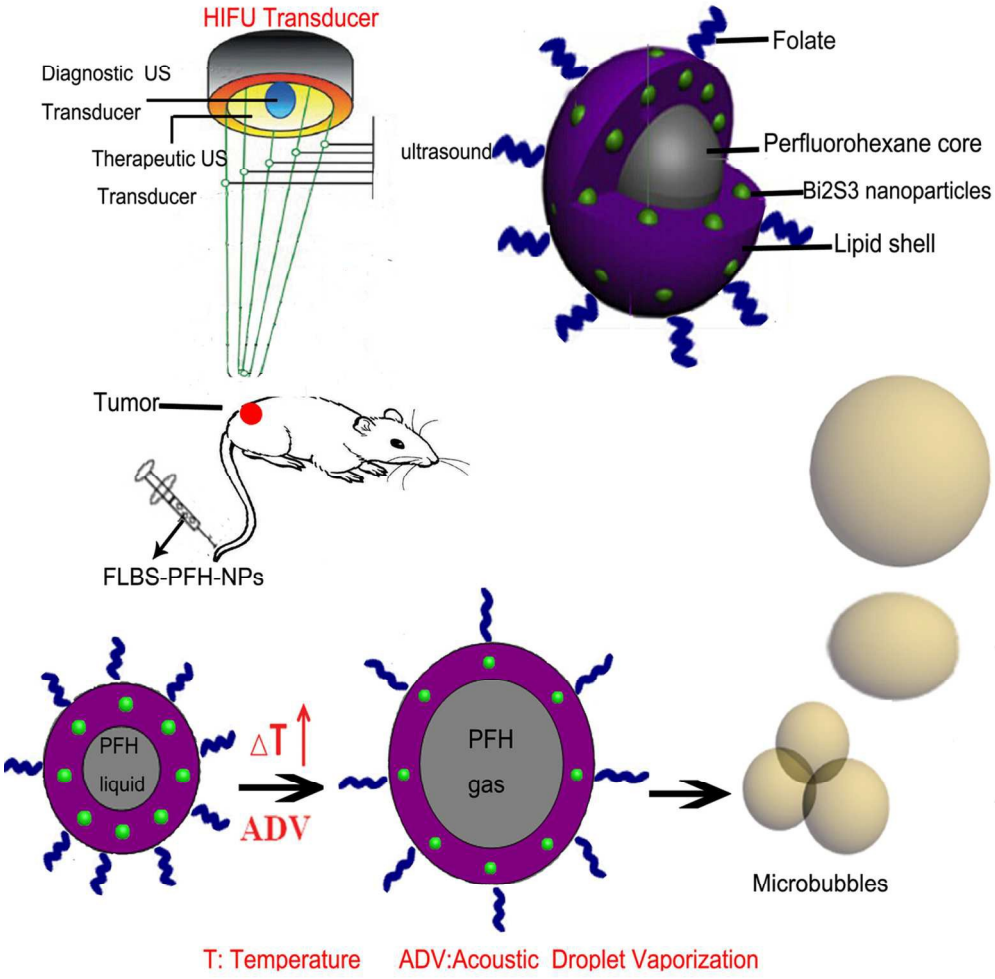

117x119mm (300 x 300 DPI)